

# Physicochemical Characterization of a New 2D Semiconductor Carbon Allotrope, C<sub>16</sub>: An Investigation via Density Functional Theory and Machine Learning-based Molecular Dynamics

Kleuton A. L. Lima,<sup>†</sup> Rodrigo A. F. Alves,<sup>‡,¶</sup> Elie A. Moujaes,<sup>§</sup> Alexandre C. Dias,<sup>‡,||</sup> Douglas S. Galvão,<sup>†</sup> Marcelo L. Pereira, Jr.,<sup>⊥</sup> and Luiz A. Ribeiro, Jr.\*<sup>‡,¶</sup>

<sup>†</sup>*Department of Applied Physics and Center for Computational Engineering and Sciences, State University of Campinas, Campinas, São Paulo, 13083-859, Brazil.*

<sup>‡</sup>*Institute of Physics, University of Brasília, Brasília, 70910-900, Brazil*

<sup>¶</sup>*Computational Materials Laboratory, LCCMat, Institute of Physics, University of Brasília, 70910-900, Brasília, Brazil*

<sup>§</sup>*Physics Department, Federal University of Rondônia, 76801-974, Porto Velho, Brazil*

<sup>||</sup>*International Center of Physics, University of Brasília, Brasília, 70910-900, Brazil*

<sup>⊥</sup>*University of Brasília, College of Technology, Department of Electrical Engineering, 70919-970, Brasília, Federal District, Brazil.*

E-mail: [ribeirojr@unb.br](mailto:ribeirojr@unb.br)

## Abstract

This study comprehensively characterizes, with suggested applications, a novel two-dimensional carbon allotrope, C<sub>16</sub>, using Density Functional Theory and machine learning-based molecular dynamics. This nanomaterial is derived from naphthalene and bicyclopropylidene molecules, forming a planar configuration with sp<sup>2</sup> hybridization and featuring 3-, 4-, 6-, 8-, and 10-membered rings. Cohesive energy of -7.1 eV/atom, absence of imaginary frequencies in the phonon spectrum, and the retention of the system's topology after ab initio molecular dynamics simulations confirm the structural stability of C<sub>16</sub>. The nanomaterial exhibits a semiconducting behavior with a direct band gap of 0.59 eV and anisotropic optical absorption in the  $y$  direction. Assuming a complete absorption of incident light, it registers a power conversion efficiency of 13%, demonstrating relatively good potential for applications in solar energy conversion. The thermoelectric figure of merit ( $zT$ )

reaches 0.8 at elevated temperatures, indicating a reasonable ability to convert a temperature gradient into electrical power. Additionally, C<sub>16</sub> demonstrates high mechanical strength, with Young's modulus values of 500 GPa and 630 GPa in the  $x$  and  $y$  directions, respectively. Insights into the electronic, optical, thermoelectric, and mechanical properties of C<sub>16</sub> reveal its promising capability for energy conversion applications.

## Keywords

Physicochemical Characterization; 2D Semiconductor Carbon Allotrope; Density Functional Theory; Machine Learning-based Reactive Molecular Dynamics; Excitons, Photovoltaics.

## 1 Introduction

The fabrication of new nanomaterials has always been associated with technological

progress. Advancing nanotechnology requires a deep understanding of nanomaterials.<sup>1</sup> Nanomaterials can exist at different dimensionalities, from zero (quantum dots) to three dimensions (such as diamonds). In particular, two-dimensional (2D) materials have recently attracted significant attention due to their properties and potential applications in various technological fields,<sup>2</sup> including electronics,<sup>3</sup> optoelectronics,<sup>4</sup> and energy storage.<sup>5</sup>

Since the experimental realization of graphene,<sup>6</sup> more than two decades ago, the investigation of new carbon allotropes and other 2D materials has been at the forefront of materials science. Graphene is a semimetal material<sup>7</sup> with high tensile strength<sup>8</sup> and elevated thermal stability<sup>9</sup>. These attractive properties have motivated the search for new materials with similar or improved properties.<sup>10</sup>

Among the growing number of 2D materials families, carbon allotropes are particularly promising due to carbon's ability to form multiple bonding configurations (sp, sp<sup>2</sup>, and sp<sup>3</sup> hybridizations and combinations of them),<sup>11</sup> resulting in a large diversity of physical characteristics dependent on the structural topology of atomic arrangements.<sup>12</sup> Although graphene exhibits high electrical conductivity, it has a zero electronic bandgap, limiting some kinds of applications.<sup>13</sup> This limitation has stimulated research into new 2D carbon allotropes that combine graphene's structural benefits with semiconducting properties.<sup>14</sup>

This growing interest in carbon-based 2D systems has led to the discovery and/or proposal of several new allotropes with distinct characteristics. Although most of these structures are from theoretical predictions<sup>12,15-19</sup>, significant advances have recently been made in the synthesis routes of these nanomaterials.

In addition to graphene,<sup>6</sup> fullerenes,<sup>20</sup> and carbon nanotubes,<sup>21</sup> which were synthesized years ago, recent experimental realizations include Biphenylene Network (BPN),<sup>22</sup> Holey Graphyne (HGY),<sup>23</sup>  $\gamma$ -graphyne ( $\gamma$ -GY),<sup>24-26</sup> and monolayer fullerene Network (2D-C<sub>60</sub>)<sup>27</sup>. Importantly,

these systems were theoretically predicted before their synthesis<sup>28-31</sup>

Among these 2D carbon-based systems, graphene and BPN exhibit metallic behavior, while the HGY, 2D-C<sub>60</sub>, and  $\gamma$ -GY monolayers are semiconductors.

In our quest to discover new 2D carbon allotropes, our groups have recently characterized 30 two-dimensional structures with semiconducting properties, specifically focusing on their solar energy conversion capabilities. Our results demonstrate that power conversion efficiency (PCE) values range from 7% to 30%, with the possibility of complete absorption of an incident light.<sup>32</sup> Beyond their main use in electronic devices, these 2D semiconducting carbon allotropes also appear to be promising candidates for renewable energy applications.<sup>33</sup>

In this context, in this work, we propose a new carbon allotrope named C<sub>16</sub>. Density Functional Theory (DFT) simulations were used to characterize its dynamical and thermal stability, electronic structure, and optical, excitonic, and thermoelectric properties.

We have also performed classical molecular dynamics (MD) simulations to study its mechanical properties. For the description of the inter-atomic interactions, we have employed a reactive force field trained using Machine Learning protocols based on the data obtained from ab initio Molecular Dynamics (AIMD) simulations for representative structures related to C<sub>16</sub>.

Our results show that C<sub>16</sub> is dynamically and structurally stable, with no imaginary frequencies in its phonon spectrum. It is also thermally stable, as no phase changes were observed when subjected to a thermal bath at 1000 K. C<sub>16</sub> exhibits a semiconducting behavior, with a direct electronic bandgap of 0.59 eV. Regarding its optical properties, C<sub>16</sub> exhibits anisotropic characteristics, with the main absorption activity occurring along one specific direction of the system. It has an exciton binding energy of approximately 96 meV, a power conversion efficiency (PCE) of 13%, and a figure of merit of 0.8. Regarding its mechanical properties, our results suggest an anisotropic behavior, with Young's modulus ranging from 500 GPa

to 630 GPa, depending on the direction of deformation.

## 2 Methodology

To better present the selected computational methods and simulation parameters, we have divided this section into three subsections: the modeling of  $C_{16}$ , the first-principles calculations, and the aspects of classical MD simulations.

### 2.1 System Modeling

The proposition of new nanomaterials based on carbon or other systems can have different approaches. A common approach, also used frequently in experimental processes, is to start with known hydrocarbon molecular motifs and dihydrogenated them to induce reactions.

In the literature, several structures have been obtained through the aforementioned process. Examples include the BPN and 2D- $C_{60}$  networks, which are obtained through the covalent bonding of BPN and  $C_{60}$  molecules, respectively.<sup>22,27</sup> For  $\gamma$ -GY, several small molecules can be used, particularly dehydrobenzoannulenes (DBAs).<sup>34</sup> This approach has been used for several proposed carbon monolayers, such as PAI-G,<sup>35</sup> PSI-G,<sup>36</sup> PCF,<sup>37</sup> Naphthylene,<sup>38</sup> DHQ,<sup>39</sup> TH-GY,<sup>40</sup> Nanoporous Graphene,<sup>41</sup> among others.

In this perspective, here we propose a new allotrope, which consists of one possible 'fusion' of the naphthalene<sup>42</sup> and bicyclopropylidene<sup>43</sup> into a 2D structure that is also planar (like the molecules), see Fig. 1. The molecular motifs are shown in Fig. 1(a-b). Naphthalene is an oligoacene with ten carbons, with the formula  $C_{10}H_8$ , while bicyclopropylidene is a tetrasubstituted alkene with the formula  $C_6H_8$ .

The molecules were arranged in alternating linear blocks, forming covalent bonds. The system was designed to exhibit fully  $sp^2$  hybridization. Fig. 1(c) shows a supercell of the system obtained from this process, with the molecular motifs

highlighted in blue and green. The obtained structure ( $C_{16}$ ) consists of carbon fused rings with 3, 4, 6, 8, and 10 atoms. The unit cell ( $rC_{16}$ ) contains 16 carbon atoms, Fig. 1(d).

### 2.2 First Principles Calculations

To characterize the physicochemical properties of  $C_{16}$ , we carried out first-principles simulations within the DFT formalism using the Vienna Ab initio Simulation Package (VASP).<sup>44,45</sup> The Kohn-Sham (KS) equations were solved via the projector augmented wave (PAW) method,<sup>46</sup> applying a plane-wave cutoff energy of 868.00 eV. We used the Generalized Gradient Approximation (GGA) with the Perdew-Burke-Ernzerhof (PBE) exchange-correlation functional,<sup>47</sup> enforcing a convergence criterion of 0.01 eV/Å for minimizing atomic forces and the stress tensor.

After the geometry optimization (unit cell parameters and atomic positions), we obtained the  $C_{16}$  electronic properties with a cutoff energy of 488.23 eV adopting a total energy convergence criterion of  $10^{-6}$  eV to ensure self-consistency in the electronic density. Due to systematic errors associated with the PBE functional in estimating the electronic bandgap value<sup>48,49</sup>, we applied the HSE06 hybrid exchange-correlation functional<sup>50,51</sup> for a more realistic estimation of the electronic and optical gaps. To avoid spurious interactions between the monolayer and its periodic images along the  $z$ -direction, a vacuum buffer space of 30 Å was used.

In all calculations, the  $k$ -meshes were generated automatically using the Monkhorst-Pack method,<sup>52</sup> ensuring a density of  $40 \text{ \AA}^{-1}$  along the in-plane lattice vector directions,<sup>53</sup> which results in a  $6 \times 6 \times 1$   $k$ -mesh for the unit cell. Dynamic stability was assessed by obtaining the phonon dispersion spectrum of a  $3 \times 3 \times 1$  supercell with 64 atoms, with the same convergence criteria mentioned above. To evaluate the thermal stability, we performed AIMD simulations under the canonical NVT ensemble, using a Nosé-Hoover thermostat<sup>54</sup> to control the temperature

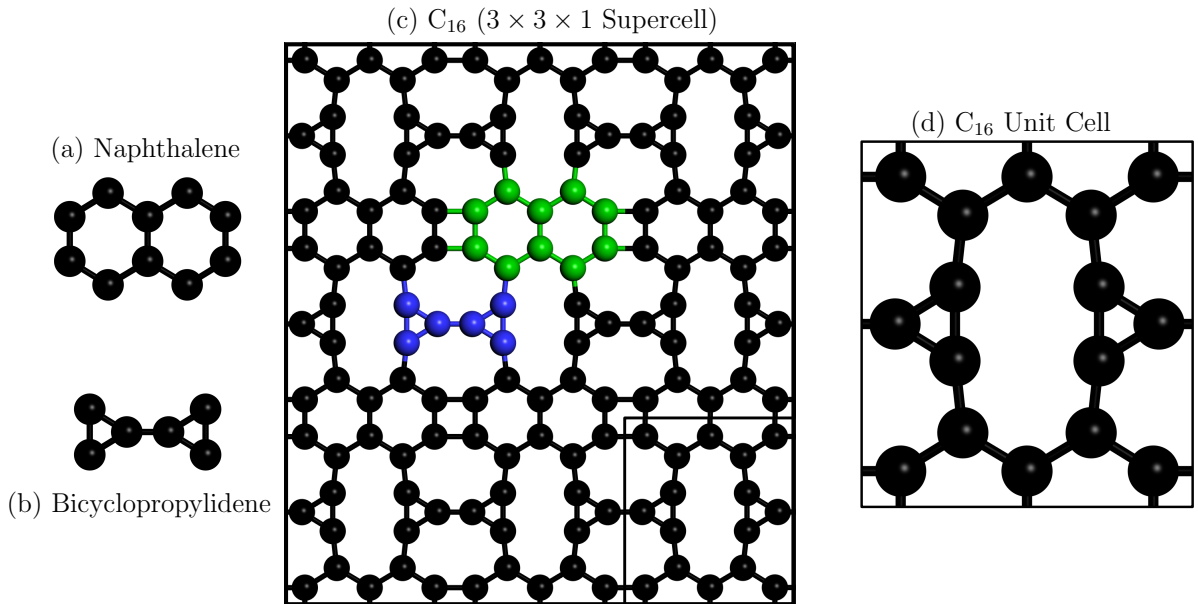


**Figure 1** Schematic representation of the proposed  $C_{16}$  structure, showing the molecules of (a) Naphthalene and (b) Bicyclopropylidene, which can be considered as the  $C_{16}$  structural building blocks. (c) a  $3 \times 3 \times 1$   $C_{16}$  supercell, with the molecular motifs highlighted in green and blue. (d)  $C_{16}$  structural unit cell.

value set at 1000 K, with a time step of 1 fs for a total simulation time of 5 ps.

To investigate the excitonic and optical properties, we used a maximally localized Wannier function tight-binding (MLWF-TB)<sup>55,56</sup> Hamiltonian to solve the Bethe-Salpeter equation (BSE),<sup>57</sup> due to the high computational cost of GW+BSE *ab-initio* approaches.<sup>58,59</sup> To determine MLWF-TB, through the Wannier90 code<sup>55,60,61</sup> we choose the C s- and p-orbital projections, based on the electronic density of states results, complemented with a random basis to achieve the same number of calculated bands in the DFT simulations.

The optical properties were analyzed at both the BSE level, which includes excitonic effects, and the independent particle approximation (IPA), which does not take into account the quasi-particle effects. These analyses were carried out using the WanTiBEXOS code.<sup>56</sup> The BSE was solved using a 2D-truncated Coulomb Potential (V2DT)<sup>62</sup> and a  $k$ -mesh of  $19 \times 17 \times 1$ ; the highest two valence bands and the lowest three conduction bands were considered in the calculations to obtain an accurate description of the optical properties in the solar emission range (i.e. 0.5 eV to 4.0 eV). To ensure accurate results, we applied a

smearing of 0.01 eV to the dielectric functions at both the BSE and IPA levels.

The thermoelectric properties, namely the Seebeck coefficient, electronic conductivity, and thermal electronic conductivity, were computed using the Boltzmann code.<sup>63</sup> This tool is interfaced with the VASP code within the Wannier90 package and depends on correctly producing the DFT-based band structure using MLWFs.<sup>64,65</sup> Convergence is achieved by choosing a coarse  $24 \times 24 \times 1$  electronic grid for self-consistent calculations and a very dense  $220 \times 220 \times 1$  electronic grid for the subsequent thermoelectric calculations.

### 2.3 Classical Molecular Dynamics Simulations

For the analysis of the  $C_{16}$  mechanical properties, we adopted an advanced approach based on machine learning interatomic potentials (MLIP).<sup>66</sup> These potentials have been proven highly effective in overcoming the limitations of more standard methods, such as empirical interatomic potentials (EIP).<sup>67</sup> MLIPs enable the integration of *ab initio* methods with classical MD simulations, allowing for

a detailed investigation of mechanical responses and fracture mechanisms in diverse materials, using interatomic potentials obtained explicitly for the investigated-like systems.

Here, we developed a specific force field for  $C_{16}$  based on the moment tensor potential (MTP),<sup>68</sup> trained with data generated from AIMD simulations in VASP. These molecular dynamics simulations were performed on supercells containing 64 atoms, covering uniaxial and biaxial strain changes to reduce the high correlation among the training data. Additionally, dynamics with progressive heating (heat ramps) were considered, resulting in 6500 training data points. This approach has been extensively validated in the literature, demonstrating success in predicting the mechanical properties of several nanomaterials.<sup>40,69,70</sup>

For MD simulations using the trained MLIP, we employed the LAMMPS software (Large-scale Atomic/Molecular Massively Parallel Simulator),<sup>71</sup>. We have used the Velocity-Verlet algorithm to integrate Newton’s equations of motion,<sup>72</sup> with a time step of 0.05 fs. After optimizing the systems using the obtained MLIP, we carried out two additional steps to the structures for the tensile loading simulations. The release of any residual stresses was controlled through simulations in an isobaric-isothermal (NPT) ensemble for 100 ps, using a Nosé-Hoover thermostat<sup>73</sup> to ensure thermal equilibrium and control. The temperature was set to 300 K and the external pressure to zero. For further tests and/or comparisons, another simulation run for an additional 100 ps was performed using a canonical ensemble (NVT) at ambient temperature.

The elastic properties and fracture patterns were evaluated at 300 K, applying a uniaxial strain rate of  $10^{-6} \text{ fs}^{-1}$  along the  $x$  and  $y$  directions separately. The system was considered periodic in all directions, with pressure adjustments made perpendicular to the direction of the strain. The stress was calculated using the stress tensor for each atom, considering the virial contributions and atomic mass. Since the system is two-dimensional, the volume was defined based on the dimensions  $L_x$  and  $L_y$ , adopting

a thickness of  $3.35 \text{ \AA}$ , consistent with the literature.<sup>74</sup>

## 3 Results and Discussion

This section examines the physicochemical properties of  $C_{16}$  based on the simulations using the abovementioned methodologies. We have explored its structural characteristics, including energy stability, dynamics, and thermal properties. Additionally, we investigated its electronic, excitonic, optical, thermoelectric, and mechanical properties. Potential applications of  $C_{16}$ , such as in solar cells, are also discussed.

### 3.1 Structural Stability

After the DFT geometry optimization, we observed that  $C_{16}$  remains in a fully planar conformation (purely  $sp^2$  hybridization). The symmetric triangular rings have one bond length of  $1.44 \text{ \AA}$ , shared with the 10-membered ring. The other two equal sides of the triangular rings have bond lengths of  $1.38 \text{ \AA}$ , shared with the 8-membered rings. The corresponding bond angle values are  $58.43^\circ$  and  $63.14^\circ$ , respectively.

The 4-membered ring is a rectangle with one side with a bond length of  $1.41 \text{ \AA}$  (shared with the hexagonal rings) and the other with  $1.54 \text{ \AA}$  (shared with the octagonal rings). The bond angle values of the benzene rings vary from  $117.5^\circ$  to  $120.8^\circ$ . For the octagonal rings, the bond angle values range from  $115.4^\circ$  to  $148.4^\circ$ , while for the decagon ring, the values vary from  $118.4^\circ$  to  $173.7^\circ$ . The  $C_{16}$  lattice vectors are  $6.48 \text{ \AA}$  and  $7.15 \text{ \AA}$  for the horizontal and vertical directions, respectively.  $C_{16}$  belongs to the  $Pmmm$  ( $D_{2h}^1$ ) symmetry group.

To determine the  $C_{16}$  stability, we have calculated the cohesive energy value,  $E_{\text{coh/atom}} = (E_{\text{tot}} - 16 \cdot E_C)/16 = -7.1 \text{ eV/atom}$ . The dynamical structural stability was verified by calculating the phonon dispersion band structure using density functional perturbation theory (DFPT) and MTP. The results are consistent and presented in Fig. 2. There is a close

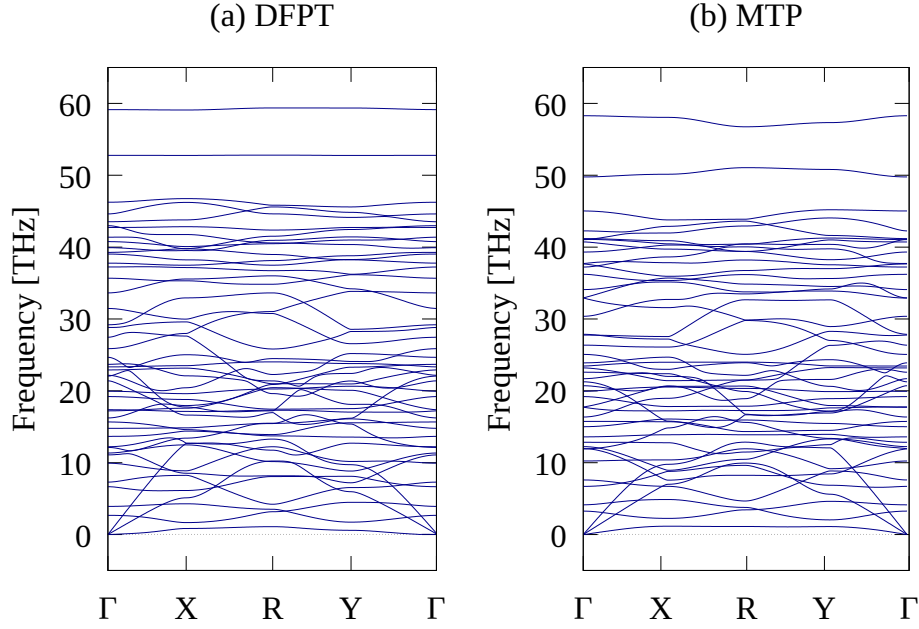


**Figure 2** Phonon dispersion spectrum of the  $C_{16}$  monolayer obtained using (a) DFPT and (b) MTP.

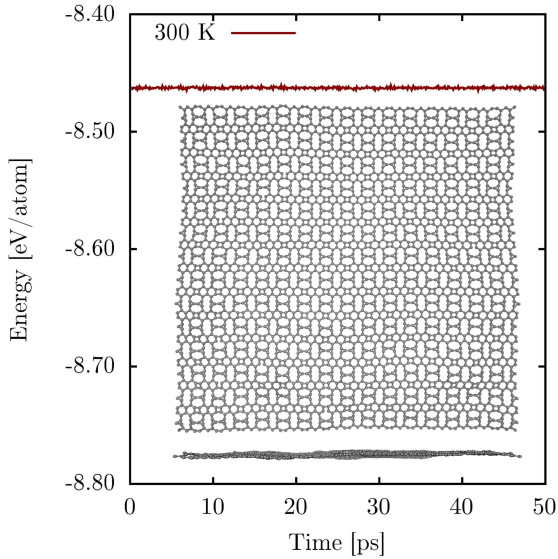


**Figure 3**  $C_{16}$  total energy values per atom as a function of the AIMD simulation. The insets show the top and lateral views of the final snapshot.

similarity in the acoustic modes. The differences in the optical modes are more pronounced. These results validate the trained MLIP. Additionally, the absence of imaginary frequencies suggests that  $C_{16}$  is structurally stable. There are two flat modes, around 54 THz and 59 THz. The lack of vibrational modes with frequencies exceeding 60 THz are consistent with the  $sp^2$  hybridization since very high

vibrations are typically associated with an  $sp$  hybridization.

To further verify the system's stability, Fig. 3 illustrates the total energy values temporal evolution of  $C_{16}$  from an AIMD simulation carried out at a thermal bath temperature of 300 K for over a 5 ps simulation time. The results show that the system's total energy is conserved, as expected. The figure's inset presents  $C_{16}$  snapshots from front and side views, which display no signs of atomic reconfiguration, bond rearrangement, or bond breaking. Furthermore, the side view reveals no significant fluctuations other than those expected from temperature variations.

### 3.2 Electronic, Excitonic, and Optical Properties

The electronic band structure and the corresponding projected density of states (PDOS) are presented in Fig. 4 (a)-(b), respectively. Our system has a direct HSE06 (PBE) band gap of 0.59 eV (0.36 eV) localized close to the Y high-symmetry point within the Y- $\Gamma$  path. From the PDOS, we can observe that the main orbital contributions around the Fermi level come from the C  $p$ -orbitals, complemented by a minimal contribution of the C  $s$ -orbitals within the

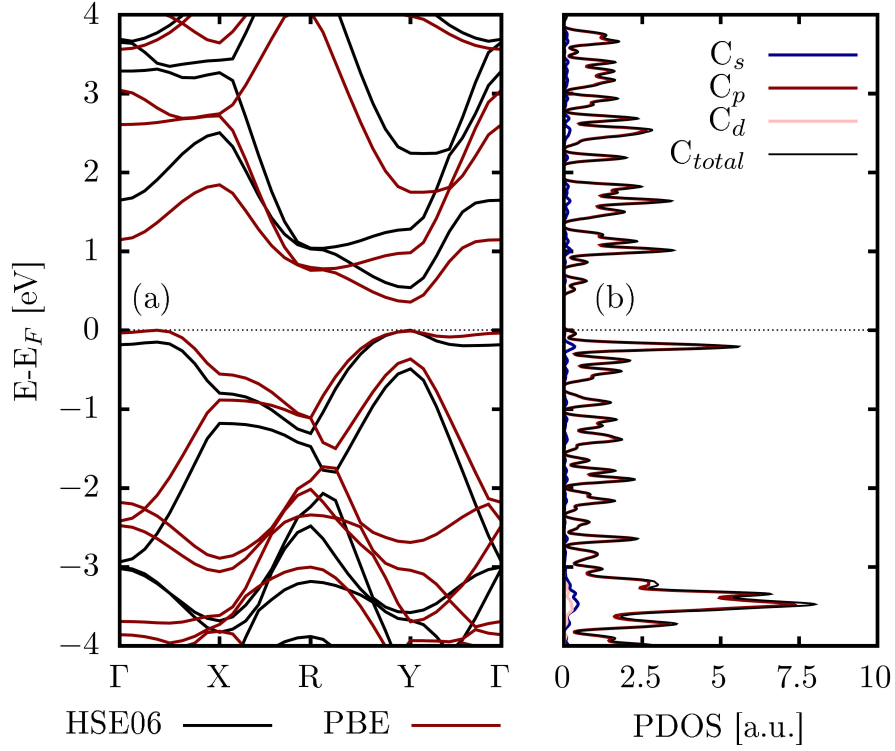


**Figure 4** (a)  $C_{16}$  electronic band Structure at the PBE (red curves) and HSE06 (black curves) levels and (b) the HSE06 Projected Density of States on the  $s$ -,  $p$ -, and  $d$ -orbitals. The Fermi level is set at 0 eV.

region close to the valence band maximum (VBM).

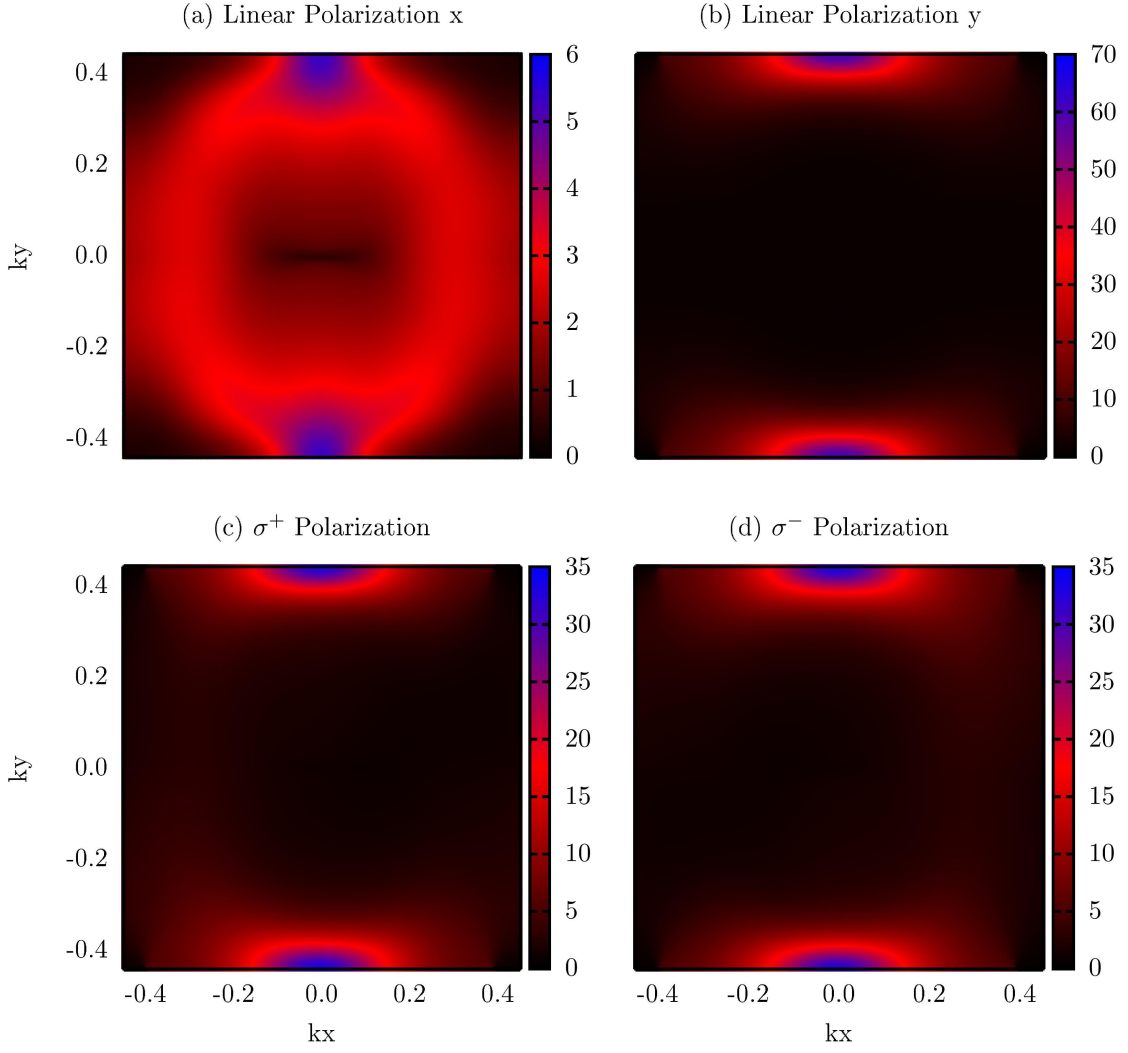
The optical activity, derived from the sum of the overall optical transitions by considering the two highest valence bands and the three lowest conduction bands, was analyzed for linear and circularly polarized light at the IPA level. This information is illustrated in Fig. 5 (a)-(d). For linear polarized light along the  $\hat{x}$  direction (Fig. 5 (a)) we have some optical activity in the entire Brillouin zone (BZ), with higher values at the BZ edges at  $k_x=0 \text{ \AA}^{-1}$  and  $k_y=\pm 0.4 \text{ \AA}^{-1}$ , respectively, with a maximum oscillator force of  $6 \text{ \AA}^2$ . When comparing the optical activity for the  $\hat{y}$  polarization, shown in Fig. 5 (b), the maximum values are in the same region of the previous panel; however, the oscillator force values are 10 times higher ( $\sim 70 \text{ \AA}^2$ ), with the optical activity concentrated at the BZ edges. These results show a large optical anisotropy, with the optical response much more intense along the  $\hat{y}$  direction.

Fig. 5 (c)-(d) illustrate the optical activity for circular light polarization, obtained from

a linear combination of  $\hat{x}$  and  $\hat{y}$  linear polarizations. The isotropic behavior shown in this case results from the dominant optical activity for the  $\hat{y}$  polarization, as the  $\hat{x}$  contribution is much smaller, resulting in practically the same linear optical response under optical helicity.

The lowest energy excitonic levels, for direct (at  $\Gamma$ ) and indirect (any other  $\mathbf{k}$ -points) excitons, are shown in Fig. 6, the  $x$ -axis representing the excitonic momentum along the  $\mathbf{k}$ -path, passing through the high symmetry points in the BZ. The excitonic ground state is direct, evidenced by the direct band gap observed in the electronic band structure. When compared with the fundamental electronic band gap, it results in an exciton binding energy of 96 meV, which is higher if compared to bulk values but lies within the lower limit for 2D carbon allotropes, where the expected exciton binding energy resides in the range [80 meV to 500 meV].<sup>32</sup>

The linear optical response, at the IPA and BSE levels considering linear and circular light polarizations, through the evaluation of the absorption coefficient, refractive index,



**Figure 5** The optical activity of  $C_{16}$  in the first Brillouin zone considering linear (a,b) and circular polarized light (c,d).

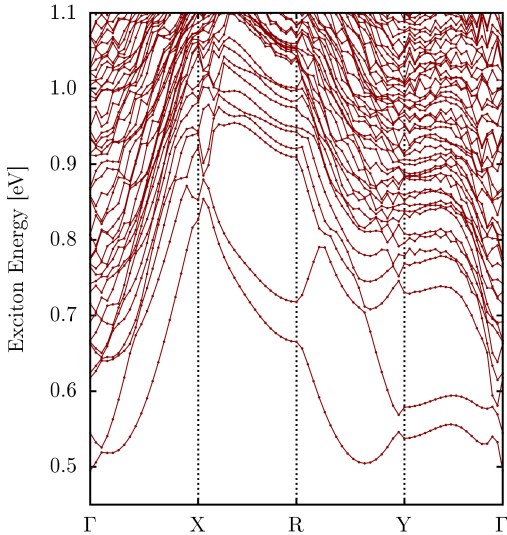


**Figure 6**  $C_{16}$  excitonic band structure obtained using an HSE06 parametrization in a MLWF-TB model.

and reflectivity is shown in Fig. 7(a)-(f). Fig. 7 (a) and (d)) demonstrate that  $C_{16}$  excitonic band structure obtained using an HSE06 parametrization in an MLWF-TB model absorbs in the infrared, visible, and ultraviolet regions. The excitonic effects result in a slight red shift in the absorption's peaks. We also observe a substantial change in the linear optical response, giving rise to an important optical anisotropy for linear light polarization because the absorption coefficient is much more intense for light polarization along the  $\hat{y}$  direction. This result is consistent with the optical activity shown in Fig. 5. In contrast, for light excitations above 3.0 eV, the absorption coefficient is much more intense for  $\hat{x}$  light polarization. The optical response is isotropic for circular light polarization for the above-mentioned reasons.

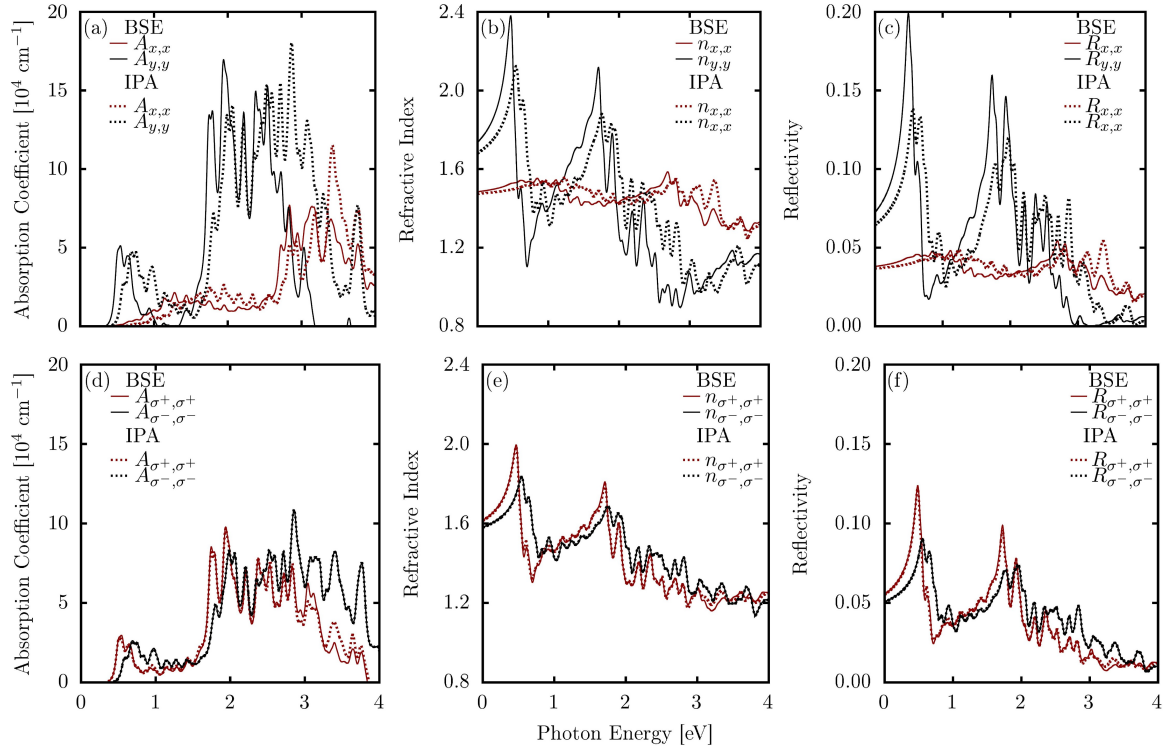


**Figure 7 (a,d) Absorption Coefficient, (b,e) Refractive Index, and (c,f) Reflectivity, calculated within the BSE (solid curves) and IPA (dashed curves) approximations for linear (a-c) and circular light polarization (d-f). Red (black) curves correspond to  $\hat{x}$  ( $\sigma^+$ ) and  $\hat{y}$  ( $\sigma^-$ ) linearly (circularly) polarized light cases.**

The optical anisotropy, under linear light polarization and the isotropic behavior for the circular one, is also seen in the refractive index (Fig. 7 (b) and (e)) and the reflectivity (Fig. 7 (c) and (f)). Under linear light polarization, the refractive index is higher for the  $\hat{y}$  polarization in the infrared and visible spectrum regions. In the ultraviolet region, it is more pronounced for the  $\hat{x}$  polarization. This index varies in the range of 0.9 to 2.4 and 1.28 to 2.4 for the  $\hat{y}$  and  $\hat{x}$  polarizations, respectively. This range is slightly narrowed when excitonic effects are considered (BSE level).

This behavior is similar to reflectivity that lies in the range of 0% to 20% for the  $\hat{y}$  polarization case and 3% to 5% for the  $\hat{x}$  polarization case. It is also interesting to observe that none of the incident photons are reflected for  $\hat{y}$  polarization in the ultraviolet region. When circular light polarizations are considered, both refractive index and reflectivity are the same, independent of clockwise ( $\sigma_-$ ) or counterclockwise ( $\sigma_+$ ) light polarization.

We can estimate the  $C_{16}$  solar harvesting

efficiency through the electronic and optical properties data, using the power conversion efficiency (PCE) as a descriptor. The PCE was obtained by two methods: the Shockley–Queisser limit (SQ)<sup>75</sup> and the spectroscopy limited maximum efficiency (SLME).<sup>76</sup> The former is directly obtained by the fundamental electronic band gap  $E_g$  when excitonic effects are not considered or through the exciton ground state energy  $Ex_{gs}$ ; this kind of approach considers that all photons with energies equal or higher than  $E_g$  or  $Ex_{gs}$  are absorbed. The latter approach, which goes beyond  $E_g$  and  $Ex_{gs}$ , also considers the optical band gap or the exciton bright ground state energy when the excitonic effects are taken into account. Here, the absorption spectrum and the material thickness are the two fundamental parameters needed to estimate the optical absorbance that provides the incident photon absorption rate. For 2D materials, the value of van der Waals length (3.21 Å) is added. This procedure is based on the work of Bernardi *et al.*,<sup>77</sup> where it was used to estimate graphene's absorbance due

to its atomic thickness, providing results consistent with experimental data. For both approaches, the PCE was also estimated considering the solar cell at 300K and considering the AM1.5G model for the solar emission spectrum.<sup>78</sup> It is equally important to understand that both methods provide an upper limit of the solar harvesting efficiency and that experimentally reaching these values can demand years of research. Details of the theoretical formalism behind both methods can be found in previous works.<sup>56,79</sup>

The SQ-limit estimates a  $PCE^{SQ}$  of 17.06 % when excitonic effects are not considered; yet, when quasiparticle effects are taken into account, the value is reduced to 12.96 %, due to the exciton binding energy, which results in  $Ex_{gs}$ , being smaller than  $E_g$ . The SQ-Limit curve has a maximum  $PCE^{SQ}$  when either  $E_g$  or  $Ex_{gs}$  comes closer to 1.31 eV; the further  $E_g$  or  $Ex_{gs}$  are from this ideal value, the lower is  $PCE^{SQ}$ . The SLME values ( $PCE^{SLME}$ ) are significantly lower than those obtained through the previous approximation, resulting in a solar harvesting efficiency of less than 0.08 %, regardless of whether quasi-particle effects are present. This low efficiency is primarily due to the material's monolayer thickness, which leads to a poor photon absorbance rate, as most incident photons pass through the material without being absorbed. Consequently, the material is almost transparent, presenting a considerable challenge for the use of 2D monolayers in photovoltaic devices.

Based on the investigation of Jariwala and co-workers,<sup>80</sup> which proposes a solution for this problem using light trapping techniques to enhance the absorbance rate closer to 100 % in 2D materials, we made another estimation of PCE ( $PCE_{max}^{SLME}$ ), adapting the SLME method, and considering the absorbance rate as a Heaviside function, where we adopt the value of 1 for incident photons with energy equals or higher than the optical band gap or exciton bright ground state and 0 otherwise.  $PCE_{max}^{SLME}$  evaluates to an efficiency of 12.96 % with excitonic effects considered and 17.05 % when they are absent, suggesting a potential application of this

monolayer as a solar harvesting absorber if light trapping schemes are applied.

The above results are consistent with previous investigations of 2D carbon allotropes for photovoltaic applications.<sup>32</sup> It is crucial to report the performance characteristics (PCE) both with and without excitonic effects, as the exciton binding energy is highly sensitive to the surrounding dielectric environment. Excitonic effects tend to be reduced by proximity interactions when a monolayer is in contact with other materials. This scenario is particularly relevant in solar cells, where the absorber layer is sandwiched between the electron and hole transport layers, leading to experimentally lower excitonic effects. In this work, we have explored both extremes: the maximum excitonic effects, which occur when the monolayer is in a vacuum, and the complete absence of these quasi-particle effects, which provide a more realistic value for the PCE. The actual performance is expected to fall somewhere between these two extremes.

### 3.3 Thermoelectric Properties

The effectiveness of a material in thermoelectric devices is measured by probing its figure of merit ( $zT$ )<sup>81,82</sup> defined as:

$$zT = \frac{S^2\sigma}{\kappa_e + \kappa_L},$$

where  $S$  is the Seebeck coefficient and  $\sigma$  the electronic conductivity;  $\kappa_e$  and  $\kappa_L$  are the thermal electronic and thermal lattice conductivities, respectively. The quantity  $S^2\sigma$  is the so-called power factor (PF); it represents the ability to produce electrical power from temperature gradients. Within the Boltzmann transport theory,<sup>83,84</sup> the tensor components of these physical quantities, except  $\kappa_L$ , can be extracted by evaluating:

$$\kappa_e^{\alpha\beta}(E) = \sum_{n,k} \tau_{n,k} v_g^\alpha(n,k) v_g^\beta(n,k) \delta(E - E_{n,k})$$

$$\sigma^{\alpha\beta}(T, \eta) = \frac{e^2}{NV} \int \sum_{n,k} \tau_{n,k} v_g^\alpha(n,k) v_g^\beta(n,k) \times \delta(E - E_{n,k}) \left[ -\frac{\partial f(T, E, \eta)}{\partial E} \right] dE$$

$$S^{\alpha\beta}(T, \eta) = \frac{1}{eVT\sigma^{\alpha\beta}(T, \eta)} \int \kappa_e^{\alpha\beta}(E - \eta) \times \left[ -\frac{\partial f(T, E, \eta)}{\partial E} \right] dE.$$

$e$  is the electron's charge,  $T$  is temperature,  $E$  represents energy,  $N$  is the number of electronic ( $\mathbf{k}$ -points) sampled in the Brillouin zone,  $V$  is the volume of the unit cell, and  $\eta$  is the chemical potential. Moreover,  $f$  is the Fermi-Dirac distribution function,  $\delta$  is the Dirac delta function,  $E_{n,k}$  is the energy of the  $n^{\text{th}}$  band at the  $k^{\text{th}}$  wave vector, and  $\tau_{n,k}$  is the electron/hole lifetime at point  $(n,k)$  in the  $E$ - $k$  plane. Likewise,  $v_g^\alpha$  is the  $\alpha^{\text{th}}$  component of the group velocity  $v_g$ . It should be noted that  $S$  is independent of the electronic lifetime, whereas  $\sigma$  and  $\kappa_e$  are not.

The computation of  $\tau_{n,k}$  requires the knowledge of the imaginary part of the electron's self-energy, deduced by evaluating electron-phonon matrix elements on a highly dense electronic grid. Since this is a burdensome job and since one single value of  $\tau$  per carrier charge is requisite for the BoltzWann code, the electronic lifetime will be directly obtained from the mobility values of the 2D  $C_{16}$  structure ( $\mu_{2D,i}$ ) via the expression:

$$\tau_i = \frac{\mu_{2D,i} m_i^*}{e},$$

with  $i$  referring to electrons ( $e$ ) or holes ( $h$ ). Along the  $x$  and  $y$  directions,  $\mu_e > \mu_h$  and  $\tau_e > \tau_h$  at all temperatures.

On the other hand,  $\kappa_L$  is determined via:

$$\kappa_L^{\alpha\beta} = \frac{1}{NV} \sum_{\mathbf{q},s} c_v(\mathbf{q},s) v_g^\alpha(\mathbf{q},s) v_g^\beta(\mathbf{q},s) \tau(\mathbf{q},s),$$

where  $c_v$  is the phonon specific heat capacity and  $\tau(\mathbf{q},s)$  is the phonon lifetime of vibrational mode  $s$  at the  $\mathbf{q}^{\text{th}}$  (phonon) point. This calculation can be performed using the PHONO3PY code<sup>85,86</sup>, which requires the tedious evaluation of third-order

anharmonic constants. Such estimation is computationally very heavy, especially when the unit cell comprises many atoms.

As an alternative, and assuming that the acoustic phonons only participate in the heat transport in the structure, an empirical expression of  $\kappa_L$ , derived from the Slack model, could be employed:<sup>87-90</sup>

$$\kappa_L = A \frac{\bar{M} V^{1/3} \theta_{DA}^3}{\gamma^2 n^{2/3} T}.$$

Here,  $\bar{M}$  is the average atomic mass,  $n$  is the number of atoms in the unit cell,  $T$  is temperature, and  $\theta_{DA}$  is the Debye temperature of the acoustic phonon modes.

$\gamma$  is the Grüneisen parameter, which could be obtained from the PHONOPY code by running three phonon calculations, the first at the equilibrium volume and the others at slightly smaller and slightly larger volumes than the equilibrium one. Instead, it could be easily determined via an empirical expression that depends on the Poisson ratio ( $\nu$ ) of the material:<sup>90,91</sup>

$$\gamma = \frac{3}{2} \left( \frac{1 + \nu}{2 - 3\nu} \right).$$

Since  $\nu$  can be computed along any crystallographic direction,  $\gamma$  becomes direction dependent too. On the other hand,  $A$  is a coefficient inherent in the Slack expression and dependent on  $\gamma$  such that:<sup>90,92,93</sup>

$$A = \frac{2.4 \times 10^{-6}}{1 - \frac{0.514}{\gamma} + \frac{0.228}{\gamma^2}}.$$

It has been observed that such an expression overestimates the values of  $\kappa_L$  in some materials;<sup>94</sup> however, this is currently our best approach until an experimental value of  $\kappa_L$  for the  $C_{16}$  monolayer becomes available.

Fig. 8 illustrates  $C_{16}$   $S$ ,  $\sigma$ ,  $\kappa_e$ , and PF along the  $x$  and  $y$  directions for  $T = 300$  K, 600 K, and 1000 K. These quantities are plotted for chemical potential values 0.3 eV above and below the Fermi level to model electron and hole doping. For any temperature  $T$ ,  $S$  is larger along the  $x$  direction. Except for  $S$ , the curves show some minor discontinuity when  $\eta$  approaches  $E_F$  from both sides due to the

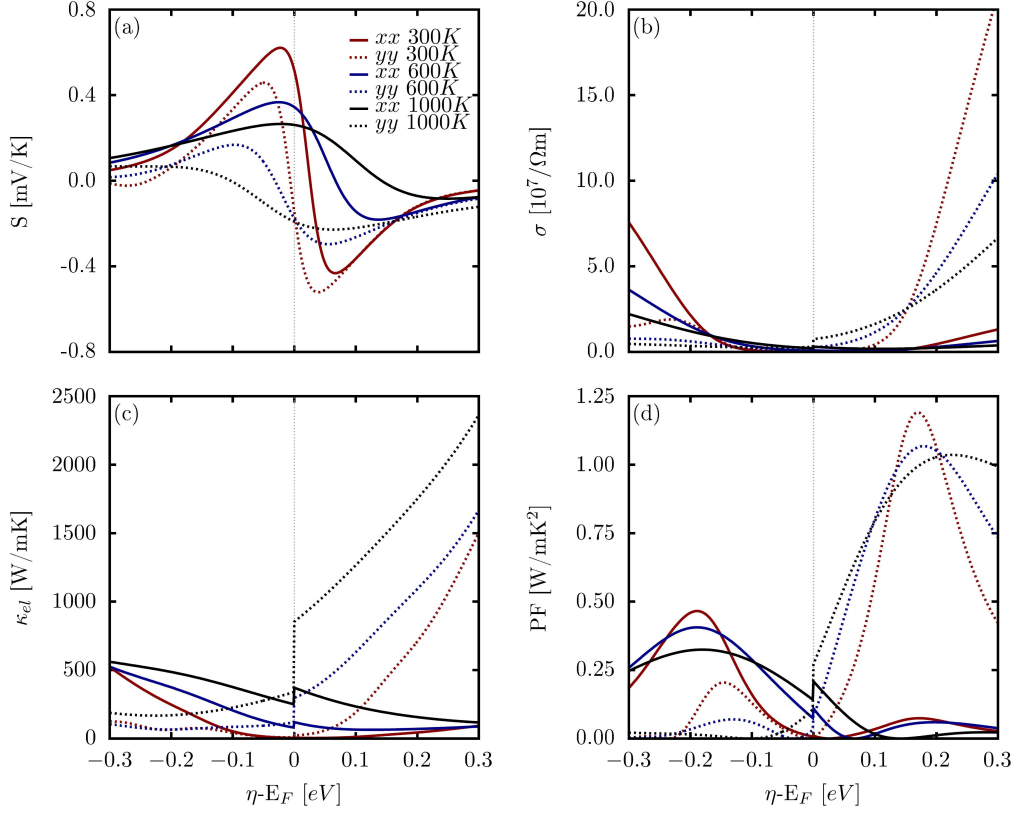


**Figure 8 (a) The change of the Seebeck coefficient, (b) the electronic conductivity, (c) the thermal electronic conductivity, and (d) the power factor as a function of electron and hole doping along the  $x$  and  $y$  directions at 300 K (red), 600 K (blue), and 1000 K (black).**

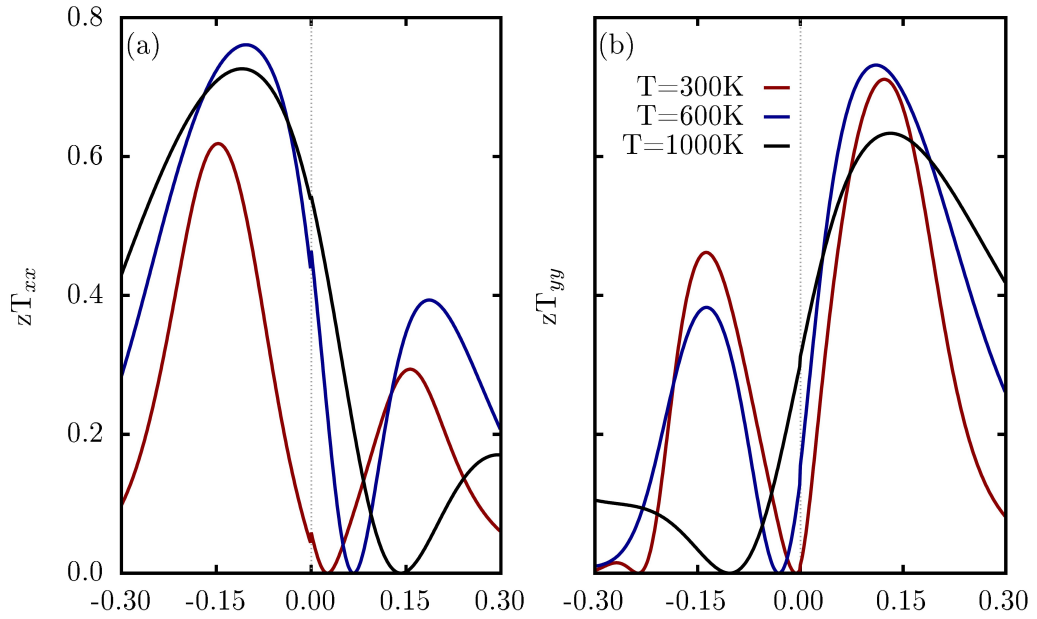


**Figure 9 Same as in Fig. 8 but for the figure of merit ( $zT$ ) at 300 K, 600 K, and 1000 K along the (a)  $x$  and (b)  $y$  directions.**

**Table 1** Calculated effective mass  $m_i^*$ , average effective mass  $m_d$ , in-plane stiffness  $C_{2D}$ , DP constant  $E_1$ , the charge carrier mobility  $\mu$ , and the electronic lifetime  $\tau$  at  $T = 300$  K, 600 K, and 1000 K for the  $C_{16}$ . Here,  $m_0$  is the mass of a free electron.

$T = 300$ K							
Direction	Carrier	$m_i^* (m_0)$	$m_d (m_0)$	$C_{2D} (eV/\text{\AA})$	$E_1 (eV)$	$\mu (10^3 \text{cm}^2 \text{V}^{-1} \text{s}^{-1})$	$\tau (ps)$
$x$	$e$	0.15	0.021	6.19	-9.95	61.2	5.227
	$h$	0.29	0.081	6.19	-8.68	21.2	3.500
$y$	$e$	0.14	0.021	7.95	6.80	180.4	14.380
	$h$	0.28	0.081	7.95	7.68	36.01	5.739
$T = 600$ K							
Direction	Carrier	$m_i^* (m_0)$	$m_d (m_0)$	$C_{2D} (eV/\text{\AA})$	$E_1 (eV)$	$\mu (10^3 \text{cm}^2 \text{V}^{-1} \text{s}^{-1})$	$\tau (ps)$
$x$	$e$	0.15	0.021	6.19	-9.95	30.6	2.613
	$y$	0.29	0.081	6.19	-8.68	10.5	1.734
$y$	$e$	0.14	0.021	7.95	6.80	90.2	7.190
	$h$	0.28	0.081	7.95	7.68	18.0	2.869
$T = 1000$ K							
Direction	Carrier	$m_i^* (m_0)$	$m_d (m_0)$	$C_{2D} (eV/\text{\AA})$	$E_1 (eV)$	$\mu (10^3 \text{cm}^2 \text{V}^{-1} \text{s}^{-1})$	$\tau (ps)$
$x$	$e$	0.15	0.021	6.19	-9.95	18.4	1.571
	$y$	0.29	0.081	6.19	-8.68	6.4	1.05
$y$	$e$	0.14	0.021	7.95	6.80	54.1	4.312
	$h$	0.28	0.081	7.95	7.68	10.8	1.722

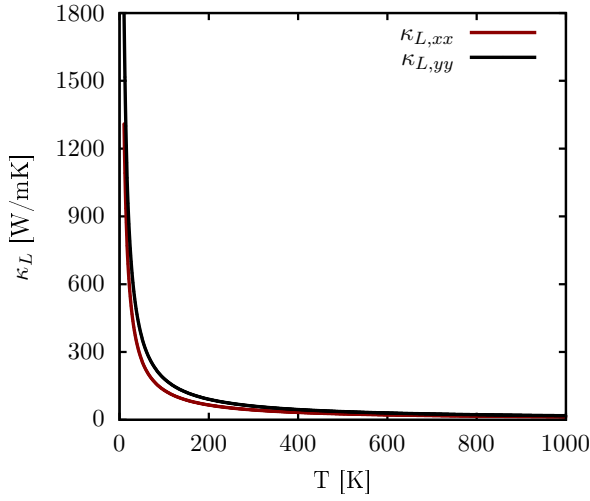


**Figure 10** Lattice thermal conductivity along the  $x$ - (red) and  $y$ -directions (black).

different electron and hole electronic lifetime values  $\tau_e$  and  $\tau_h$  (table 1) as  $\eta - E_F \rightarrow 0^+$  and  $\eta - E_F \rightarrow 0^-$ .

For the undoped  $C_{16}$ , that is for  $\eta \sim E_F$  and  $T = 300$  K,  $\kappa_e = 6.05$  W/(mK) along the  $x$  direction and  $\kappa_e = 22.79$  W/(mK) along the  $y$ -direction. These values increase as  $T$  increases, with the electronic thermal conductivity along the  $x$  direction always smaller than that along the  $y$  one. More specifically,  $\kappa_{e,xx} = 119.79$  W/(mK) and

$\kappa_{e,yy} = 296.87$  W/(mK) at  $T = 600$  K, and  $\kappa_{e,xx} = 371.14$  W/(mK) and  $\kappa_{e,yy} = 853.22$  W/(mK) at  $T = 1000$  K.

Regarding the PF, we also observed that the values along the  $x$  direction are larger than those along the  $y$  one, at least for  $T = 300$  and 600 K. At ambient temperatures,  $\text{PF}_{xx} = 9.70$  mW/(mK<sup>2</sup>) while  $\text{PF}_{yy} = 3.36$  mW/(mK<sup>2</sup>). At 600 K,  $\text{PF}_{xx}$  reaches a value of 0.11 W/(mK<sup>2</sup>) and  $\text{PF}_{yy}$  attains a value of 0.08 W/(mK<sup>2</sup>).

As can be seen from Fig. 10, the lattice thermal conductivity  $\kappa_L$  shows smaller values along the  $x$  direction. At  $T = 300$  K and for the undoped structure,  $\kappa_{L,xx} = 43.67$  W/(mK) and  $\kappa_{L,yy} = 60.67$  W/(mK). As  $T$  is increased,  $\kappa_L$  decreases such that  $\kappa_{L,xx} = 21.84$  W/(mK), and  $\kappa_{L,yy} = 30.34$  W/(mK) at 600 K, and  $\kappa_{L,xx} = 13.10$  W/(mK), and  $\kappa_{L,yy} = 18.20$  W/(mK) at 1000 K.

To achieve a significant value of  $zT$ , a maximum value of PF and a minimum value of the sum of the thermal conductivities are needed. As expected, the figure of merit along the  $x$  direction is higher. For the undoped structure,  $zT$  registers values of 0.06, 0.46, and 0.54 at  $T = 300$  K, 600 K, and 1000 K, respectively.

Since the structure is thermally stable at 1000 K, a value of  $zT = 0.54$  is relatively high; however, having  $zT$  values larger than or equal to 0.8 is desirable. Upon doping,  $zT_{xx}$  ( $zT_{yy}$ ) reaches a maximum value of 0.62 (0.71) for energies 0.15 eV (0.12 eV) below (above)  $E_F$  at ambient temperature. For  $T = 600$  K, the maxima obtained values of 0.76 (0.73) for  $zT_{xx}$  ( $zT_{yy}$ ) occurring at 0.1 eV (0.11 eV) below (above)  $E_F$ . At a higher temperature of 1000 K,  $zT_{xx}$  has a maximum of 0.73 for an energy of 0.11 eV below  $E_F$ , while  $zT_{yy}$  depicts a maximum of 0.63 for an energy of 0.13 eV above  $E_F$ .

Knowing that energies below the Fermi level correspond to hole doping while those above to electron doping and that the farther we are from  $E_F$ , the heavier the doping, our best compromise is to induce a  $p$ -doping process capable of securing a  $zT_{xx}$  of 0.76 at  $T = 600$  K, and by lowering  $E_F$  by just 0.1 eV. Considering that  $E_F$  is proportional to the electron/hole density ( $n$ ), then we can assume that  $\Delta E_F/E_{F0} = \Delta n/n_0$ , where  $E_{F0}$  and  $n_0$  are the Fermi energy and electron/hole concentration for the undoped system, respectively;  $\Delta E_F = E_F - E_{F0}$  and  $\Delta n = n - n_0$ ,  $E_F$  being the Fermi energy and  $n$  the carrier concentration of the doped system. We show that  $n/n_0 = 1.042$ , implying that  $n = 1.042n_0$ , or  $n \sim n_0$ . Thus, by just lightly doping  $C_{16}$  with holes corresponding to a 0.1 eV shift in the Fermi energy, we can reach a  $zT$  as high as 0.76 along the  $x$  direction.

### 3.4 Mechanical Properties

To understand the  $C_{16}$  mechanical response, we initially performed ab initio molecular dynamics (AIMD) simulations under various fixed strain values and with constant temperature variations. Based on these data, a machine learning interatomic potential (MLIP) was trained, which was then used to obtain the mechanical response of the system. A  $C_{16}$   $16 \times 14 \times 1$  supercell containing 3584 atoms was subjected to deformations along the  $x$  and  $y$  directions up to a maximum of 15% of the respective initial length values.

In Fig. 11, we present the stress-strain curves obtained from these simulations.

The red points represent the calculated stress for each deformation percentage along the  $x$  direction. In contrast, the blue points show the corresponding results for uniaxial deformation applied along the  $y$  direction. The system exhibits partially similar behaviors concerning hardness for these directions. Along the  $x$  direction, Young's modulus is approximately 500 GPa, while along the  $y$  one, this value reaches nearly 630 GPa. Both cases display ductile characteristics; however, the stress accumulation along the  $y$  direction is higher, leading the structure to fracture at a strain of only 5.5%. On the other hand, along the  $x$  direction, the system endures nearly a three times greater deformation, with a critical strain at 14.6%. Given these aspects, the maximum stress obtained for deformation along the  $x$  direction is approximately 61.7 GPa at 14.6% strain and 33.1 GPa along the  $y$  one at 5.5% strain.

To gain deeper insights into the  $C_{16}$  mechanical response, in Fig. 12, we present representative snapshots of  $C_{16}$  under several strain values. Panels (a) and (d) depict the system's equilibrium state after residual stresses have been eliminated and the system thermalized at room temperature. The color gradient from blue to red represents the Von Mises (VM) stress<sup>95–98</sup>, which provides a better understanding of where the fractures originate and propagate.

In panel (b), the system is shown at 14.4% strain on the limit of fracturing. The

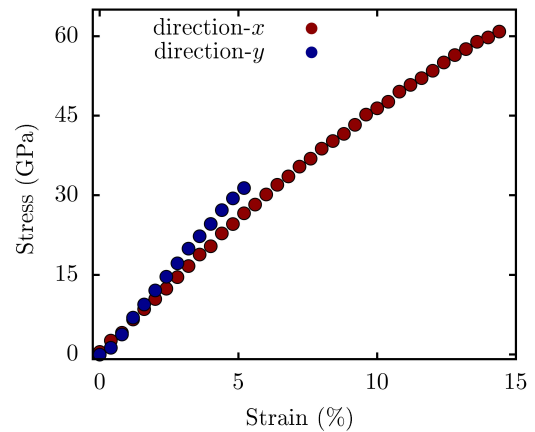


**Figure 11 Stress-Strain curve, obtained using MLIP, for strain along the  $x$ - (red) and  $y$ -directions (blue).**

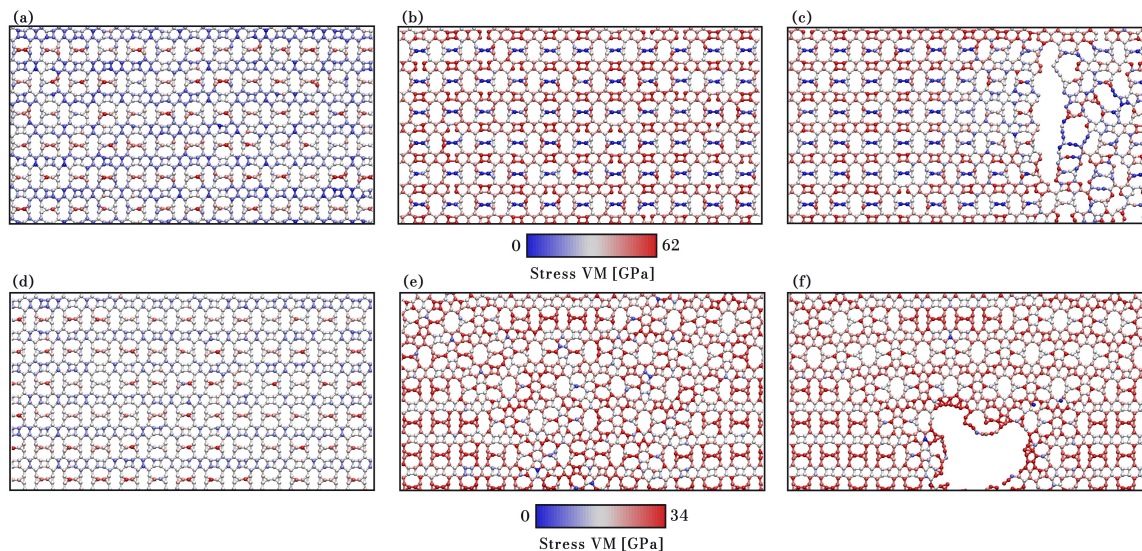


**Figure 12** Representative snapshots of the  $C_{16}$  monolayer at different stages of the deformation process along the  $x$  (a-c) and  $y$  (d-f) directions. The deformations shown are at (a) 0%, (b) 14.4%, and (c) 14.7% along the  $x$  direction, and (d) 0%, (e) 5.3%, and (f) 5.6% along the  $y$  one.

strain is concentrated in the region forming covalent chains of naphthalene, particularly in the rectangular rings, given their limited flexibility to release the strain. Finally, panel (c) shows the system at 15% strain, where the fracture occurs, and a crack propagates, with successive breakages of the hexagonal rings.

Along the  $y$  direction, panel (e) shows the system under 5% strain. Several bonds have reconfigured, and it is possible to observe that stress is concentrated mainly in the regions derived from the bicyclopropylidene molecule. This region proved to be more fragile due to the topology of the involved rings, which explains the early system failure under strain along this direction. After the atomic reconfiguration upon fracture (panel (c) – 5.6%), several bonds break, leading to the  $C_{16}$  complete structural failure.

## 4 Conclusion

In summary, we propose a new two-dimensional carbon allotrope with a semiconductor behavior. We performed first-principles simulations based on the DFT formalism and atomistic simulations using a reactive force field trained through machine learning to characterize this novel nanomaterial. We conclude that the  $C_{16}$

monolayer demonstrates promising physical and chemical properties, particularly in applications involving electronic devices and energy conversion. Electronically, 2D- $C_{16}$  displays a direct bandgap of 0.59 eV, making it suitable for optoelectronic device applications. Its optical properties demonstrate anisotropic absorption along the  $y$  direction, with the material possessing an exciton binding energy of 96 meV, confirming its potential in photovoltaic applications. The material holds a power conversion efficiency ( $PCE_{max}^{SLME}$ ) of 13% when all photons are absorbed and excitonic effects are considered. The thermoelectric figure of merit ( $zT$ ) can reach 0.8 at elevated temperatures, indicating that  $C_{16}$  can be utilized in thermoelectric devices. Additionally, the anisotropic mechanical strength of  $C_{16}$  is significant, with Young's moduli of 500 GPa for the  $x$  direction and 630 GPa for the  $y$  one, characterizing it as a ductile and robust material under mechanical stress.

**Acknowledgement** The authors are thankful for financial support from the National Council for Scientific and Technological Development (CNPq, grant numbers 408144/2022 – 0 and 305174/2023 – 1), Federal District Research Support Foundation (FAPDF, grant

numbers 00193 – 00001817/2023 – 43 and 00193 – 00002073/2023 – 84), the Coordination for Improvement of Higher Level Education (CAPES). In addition, the authors thank the “Centro Nacional de Processamento de Alto Desempenho em São Paulo” (CENAPAD-SP, UNICAMP/FINEP - MCTI project) for resources into the 897 and 570 projects, Lobo Carneiro HPC (NACAD) at the Federal University of Rio de Janeiro (UFRJ) for resources into 133 project. L.A.R.J acknowledges the financial support from FAPDF grant 0193.000942/2015, CNPq grant 350176/2022 – 1, and FAPDF-PRONEM grant 00193.00001247/2021 – 20. A.C.D. and L.A.R.J also acknowledge PDPG-FAPDF-CAPES Centro-Oeste grant number 00193 – 00000867/2024 – 94. M.L.P.J. acknowledges financial support from FAP-DF grant 00193-00001807/2023-16. Elie A. Moujaes would like to thank the financial support of the Brazilian National Council for Scientific and Technological Development CNPq, grant number 315324/2023 – 6. K.A.L.L and D.S.G. acknowledge the Center for Computing in Engineering and Sciences at Unicamp for financial support through the FAPESP/CEPID Grant #2013/08293-7.

## References

- 1 Suhag, D.; Thakur, P.; Thakur, A. Introduction to nanotechnology. *Integrated Nanomaterials and their Applications* **2023**, 1–17.
- 2 Yadav, A.; Kumar, H.; Sharma, R.; Kumari, R. Synthesis, processing, and applications of 2D (nano) materials: A sustainable approach. *Surfaces and Interfaces* **2023**, 39, 102925, DOI: [10.1016/j.surfin.2023.102925](https://doi.org/10.1016/j.surfin.2023.102925).
- 3 Alshammari, B. H.; Lashin, M. M.; Mahmood, M. A.; Al-Mubaddel, F. S.; Ilyas, N.; Rahman, N.; Sohail, M.; Khan, A.; Abdullaev, S. S.; Khan, R. Organic and inorganic nanomaterials: fabrication, properties and applications. *RSC advances* **2023**, 13, 13735–13785, DOI: [10.1039/D3RA01421E](https://doi.org/10.1039/D3RA01421E).
- 4 Lipovka, A.; Garcia, A.; Abyzova, E.; Fatkullin, M.; Song, Z.; Li, Y.; Wang, R.; Rodriguez, R. D.; Sheremet, E. Laser Processing of Emerging Nanomaterials for Optoelectronics and Photocatalysis. *Advanced Optical Materials* **2024**, 12, 2303194, DOI: [10.1002/adom.202303194](https://doi.org/10.1002/adom.202303194).
- 5 Yu, H.; Zhang, J.; Shaheen, I.; Ahmad, M.; Chen, X.; Akkinepally, B.; Hussain, I. Nature-resembled nanostructures for energy storage/conversion applications. *Journal of Industrial and Engineering Chemistry* **2024**, 129, 53–68, DOI: [10.1016/j.jiec.2023.08.041](https://doi.org/10.1016/j.jiec.2023.08.041).
- 6 Novoselov, K. S.; Geim, A. K.; Morozov, S. V.; Jiang, D.-e.; Zhang, Y.; Dubonos, S. V.; Grigorieva, I. V.; Firsov, A. A. Electric field effect in atomically thin carbon films. *science* **2004**, 306, 666–669, DOI: [10.1126/science.1102896](https://doi.org/10.1126/science.1102896).
- 7 Rao, C. e. e.; Sood, A. e.; Subrahmanyam, K. e.; Govindaraj, A. Graphene: the new two-dimensional nanomaterial. *Angewandte Chemie International Edition* **2009**, 48, 7752–7777, DOI: [10.1002/anie.200901678](https://doi.org/10.1002/anie.200901678).
- 8 Lee, C.; Wei, X.; Kysar, J. W.; Hone, J. Measurement of the elastic properties and intrinsic strength of monolayer graphene. *science* **2008**, 321, 385–388, DOI: [10.1126/science.1157996](https://doi.org/10.1126/science.1157996).
- 9 Wu, Z.-S.; Ren, W.; Gao, L.; Zhao, J.; Chen, Z.; Liu, B.; Tang, D.; Yu, B.; Jiang, C.; Cheng, H.-M. Synthesis of graphene sheets with high electrical conductivity and good thermal stability by hydrogen arc discharge exfoliation. *ACS nano* **2009**, 3, 411–417, DOI: [10.1021/nm900020u](https://doi.org/10.1021/nm900020u).
- 10 Perreault, F.; De Faria, A. F.; Elimelech, M. Environmental applications of graphene-based nanomaterials. *Chemical Society Reviews* **2015**, 44, 5861–5896, DOI: [10.1039/C5CS00021A](https://doi.org/10.1039/C5CS00021A).
- 11 Peschel, G. Carbon-carbon bonds: hybridization. <http://www.physik.fu-berlin.de/einrichtungen/ag/>

- [ag-reich/lehre/Archiv/ss2011/docs/Gina\\_Peschel-Handout.pdf](http://ag-reich/lehre/Archiv/ss2011/docs/Gina_Peschel-Handout.pdf), 2011; Accessed: 2024-10-05.
- 12 Tiwari, S. K.; Kumar, V.; Huczko, A.; Oraon, R.; Adhikari, A. D.; Nayak, G. Magical allotropes of carbon: prospects and applications. *Critical Reviews in Solid State and Materials Sciences* **2016**, *41*, 257–317, DOI: [10.1080/10408436.2015.1127206](https://doi.org/10.1080/10408436.2015.1127206).
  - 13 Chang, H.; Wu, H. Graphene-based nanomaterials: Synthesis, properties, and optical and optoelectronic applications. *Advanced Functional Materials* **2013**, *23*, 1984–1997, DOI: [10.1002/adfm.201202460](https://doi.org/10.1002/adfm.201202460).
  - 14 Nguyen, B. H.; Nguyen, V. H. Two-dimensional hexagonal semiconductors beyond graphene. *Advances in Natural Sciences: Nanoscience and Nanotechnology* **2016**, *7*, 043001, DOI: [10.1088/2043-6262/7/4/043001](https://doi.org/10.1088/2043-6262/7/4/043001).
  - 15 Falcao, E. H.; Wudl, F. Carbon allotropes: beyond graphite and diamond. *Journal of Chemical Technology & Biotechnology: International Research in Process, Environmental & Clean Technology* **2007**, *82*, 524–531, DOI: [10.1002/jctb.1693](https://doi.org/10.1002/jctb.1693).
  - 16 Zhang, R.-S.; Jiang, J.-W. The art of designing carbon allotropes. *Frontiers of Physics* **2019**, *14*, 1–17, DOI: [10.1007/s11467-018-0836-5](https://doi.org/10.1007/s11467-018-0836-5).
  - 17 Longuinhos, R.; Moujaes, E. A.; Alexandre, S. S.; Nunes, R. Theoretical chemistry of  $\alpha$ -graphyne: functionalization, symmetry breaking, and generation of dirac-fermion mass. *Chemistry of Materials* **2014**, *26*, 3701–3708, DOI: [10.1021/cm501018w](https://doi.org/10.1021/cm501018w).
  - 18 Brandão, W. H.; Aguiar, A. L.; Fonseca, A. F.; Galvão, D.; De Sousa, J. Mechanical properties of tetragraphene single-layer: A molecular dynamics study. *Mechanics of Materials* **2023**, *176*, 104503, DOI: [10.1016/j.mechmat.2022.10450](https://doi.org/10.1016/j.mechmat.2022.10450).
  - 19 Tromer, R. M.; Júnior, L. R.; Galvão, D. S.; Dias, A. C.; Moujaes, E. A. On the mechanical, thermoelectric, and excitonic properties of Tetragraphene monolayer. *Materials Today Communications* **2024**, *39*, 109310, DOI: [10.1016/j.mtcomm.2024.109310](https://doi.org/10.1016/j.mtcomm.2024.109310).
  - 20 Kroto, H. W.; Heath, J. R.; O'Brien, S. C.; Curl, R. F.; Smalley, R. E. C60: Buckminsterfullerene. *nature* **1985**, *318*, 162–163, DOI: [10.1038/318162a0](https://doi.org/10.1038/318162a0).
  - 21 Iijima, S.; Ichihashi, T. Single-shell carbon nanotubes of 1-nm diameter. *nature* **1993**, *363*, 603–605, DOI: [10.1038/363603a0](https://doi.org/10.1038/363603a0).
  - 22 Fan, Q.; Yan, L.; Tripp, M. W.; Krejčí, O.; Dimosthenous, S.; Kachel, S. R.; Chen, M.; Foster, A. S.; Koert, U.; Liljeroth, P.; others Biphenylene network: A nonbenzenoid carbon allotrope. *Science* **2021**, *372*, 852–856, DOI: [10.1126/science.abg4509](https://doi.org/10.1126/science.abg4509).
  - 23 Liu, X.; Cho, S. M.; Lin, S.; Chen, Z.; Choi, W.; Kim, Y.-M.; Yun, E.; Baek, E. H.; Lee, H.; others Constructing two-dimensional holey graphyne with unusual annulative  $\pi$ -extension. *Matter* **2022**, *5*, 2306–2318, DOI: [10.1016/j.matt.2022.04.033](https://doi.org/10.1016/j.matt.2022.04.033).
  - 24 Li, Q.; Li, Y.; Chen, Y.; Wu, L.; Yang, C.; Cui, X. Synthesis of  $\gamma$ -graphyne by mechanochemistry and its electronic structure. *Carbon* **2018**, *136*, 248–254, DOI: [10.1016/j.carbon.2018.04.081](https://doi.org/10.1016/j.carbon.2018.04.081).
  - 25 Desyatkin, V. G.; Martin, W. B.; Aliev, A. E.; Chapman, N. E.; Fonseca, A. F.; Galvão, D. S.; Miller, E. R.; Stone, K. H.; Wang, Z.; Zakhidov, D.; others Scalable synthesis and characterization of multilayer  $\gamma$ -graphyne, new carbon crystals with a small direct band gap. *Journal of the American Chemical Society* **2022**, *144*, 17999–18008, DOI: [10.1021/jacs.2c06583](https://doi.org/10.1021/jacs.2c06583).
  - 26 He, S.; Wu, B.; Xia, Z.; Guo, P.; Li, Y.; Song, S. One-pot synthesis of gamma-graphyne supported Pd nanoparticles with high catalytic activity.

- Nanoscale Advances* **2023**, *5*, 2487–2492, DOI: [10.1039/d3na00096f](https://doi.org/10.1039/d3na00096f).
- 27 Hou, L.; Cui, X.; Guan, B.; Wang, S.; Li, R.; Liu, Y.; Zhu, D.; Zheng, J. Synthesis of a monolayer fullerene network. *Nature* **2022**, *606*, 507–510, DOI: [10.1038/s41586-022-04771-5](https://doi.org/10.1038/s41586-022-04771-5).
- 28 Baughman, R.; Eckhardt, H.; Kertesz, M. Structure-property predictions for new planar forms of carbon: Layered phases containing sp<sup>2</sup> and sp atoms. *The Journal of chemical physics* **1987**, *87*, 6687–6699, DOI: [10.1063/1.453405](https://doi.org/10.1063/1.453405).
- 29 Balaban, A.; Rentia, C. C.; Ciupitu, E. Chemical graphs. 6. Estimation of relative stability of several planar and tridimensional lattices for elementary carbon. *Rev. Roum. Chim* **1968**, *13*, 231–247.
- 30 Berber, S.; Osawa, E.; Tománek, D. Rigid crystalline phases of polymerized fullerenes. *Physical Review B* **2004**, *70*, 085417, DOI: [10.1103/PhysRevB.70.085417](https://doi.org/10.1103/PhysRevB.70.085417).
- 31 Hudspeth, M. A.; Whitman, B. W.; Barone, V.; Peralta, J. E. Electronic properties of the biphenylene sheet and its one-dimensional derivatives. *ACS nano* **2010**, *4*, 4565–4570, DOI: [10.1021/nn100758h](https://doi.org/10.1021/nn100758h).
- 32 Cavaleiro Dias, A.; Almeida Cornélio, C. D.; Piotrowski, M. J.; Ribeiro Júnior, L. A.; de Oliveira Bastos, C. M.; Caldeira Rêgo, C. R.; Guedes-Sobrinho, D. Can 2D Carbon Allotropes Be Used as Photovoltaic Absorbers in Solar Harvesting Devices? *ACS Applied Energy Materials* **2024**, DOI: [10.1021/acsaem.4c01544](https://doi.org/10.1021/acsaem.4c01544).
- 33 Tang, H.; Hessel, C. M.; Wang, J.; Yang, N.; Yu, R.; Zhao, H.; Wang, D. Two-dimensional carbon leading to new photoconversion processes. *Chemical Society Reviews* **2014**, *43*, 4281–4299, DOI: [10.1039/C3CS60437C](https://doi.org/10.1039/C3CS60437C).
- 34 Li, J.; Han, Y. Artificial carbon allotrope  $\gamma$ -graphyne: Synthesis, properties, and applications. *Giant* **2023**, *13*, 100140, DOI: [10.1016/j.giant.2023.100140](https://doi.org/10.1016/j.giant.2023.100140).
- 35 Chen, X.; Bouhon, A.; Li, L.; Peeters, F. M.; Sanyal, B. PAI-graphene: A new topological semimetallic two-dimensional carbon allotrope with highly tunable anisotropic Dirac cones. *Carbon* **2020**, *170*, 477–486, DOI: [10.1016/j.carbon.2020.08.012](https://doi.org/10.1016/j.carbon.2020.08.012).
- 36 Li, X.; Wang, Q.; Jena, P.  $\psi$ -Graphene: a new metallic allotrope of planar carbon with potential applications as anode materials for lithium-ion batteries. *The journal of physical chemistry letters* **2017**, *8*, 3234–3241, DOI: [10.1021/acs.jpcclett.7b01364](https://doi.org/10.1021/acs.jpcclett.7b01364).
- 37 Shen, Y.; Yu, J.; Liu, J.; Guo, Y.; Qie, Y.; Wang, Q. PCF-graphene: a 2D sp<sup>2</sup>-hybridized carbon allotrope with a direct band gap. *The Journal of Physical Chemistry C* **2019**, *123*, 4567–4573, DOI: [10.1021/acs.jpcc.8b12205](https://doi.org/10.1021/acs.jpcc.8b12205).
- 38 Beserra, D. J. P.; Saraiva-Souza, A.; Diniz, E. M.; Fadel, M.; Meunier, V.; Girão, E. C. Naphthylene- $\gamma$ : 1D and 2D carbon allotropes based on the fusion of phenyl-and naphthyl-like groups. *Physical Review Materials* **2020**, *4*, 084003, DOI: [10.1103/PhysRevMaterials.4.084003](https://doi.org/10.1103/PhysRevMaterials.4.084003).
- 39 Wang, X.; Chen, L.; Yuan, Z.; Rong, J.; Feng, J.; Muzammil, I.; Yu, X.; Zhang, Y.; Zhan, Z. DHQ-graphene: a novel two-dimensional defective graphene for corrosion-resistant coating. *Journal of Materials Chemistry A* **2019**, *7*, 8967–8974, DOI: [10.1039/C9TA00390H](https://doi.org/10.1039/C9TA00390H).
- 40 Lima, K. A.; Alves, R. A.; da Silva, D. A.; Mendonça, F. L.; Pereira, M. L.; Ribeiro, L. A. TH-graphyne: a new porous bidimensional carbon allotrope. *Physical Chemistry Chemical Physics* **2024**, DOI: [10.1039/D4CP02923B](https://doi.org/10.1039/D4CP02923B).
- 41 Moreno, C.; Vilas-Varela, M.; Kretz, B.; Garcia-Lekue, A.; Costache, M. V.; Paradinas, M.; Panighel, M.;

- Ceballos, G.; Valenzuela, S. O.; Peña, D.; others Bottom-up synthesis of multifunctional nanoporous graphene. *Science* **2018**, *360*, 199–203, DOI: [10.1126/science.aar2009](https://doi.org/10.1126/science.aar2009).
- 42 Parker, D. S.; Zhang, F.; Kim, Y. S.; Kaiser, R. I.; Landera, A.; Kislov, V. V.; Mebel, A. M.; Tielens, A. Low temperature formation of naphthalene and its role in the synthesis of PAHs (polycyclic aromatic hydrocarbons) in the interstellar medium. *Proceedings of the National Academy of Sciences* **2012**, *109*, 53–58, DOI: [10.1073/pnas.1113827108](https://doi.org/10.1073/pnas.1113827108).
- 43 de Meijere, A.; Kozhushkov, S. I.; Khlebnikov, A. F. Bicyclopropylidene—A Unique Tetrasubstituted Alkene and a Versatile C 6-Building Block. *Small Ring Compounds in Organic Synthesis VI* **2000**, 89–147, DOI: [10.1351/pac200072091745](https://doi.org/10.1351/pac200072091745).
- 44 Kresse, G.; Hafner, J. *Ab initio* Molecular Dynamics for Open-Shell Transition Metals. *Phys. Rev. B* **1993**, *48*, 13115–13118, DOI: [10.1103/physrevb.48.13115](https://doi.org/10.1103/physrevb.48.13115).
- 45 Kresse, G.; Furthmüller, J. Efficient Iterative Schemes For *Ab Initio* Total-Energy Calculations Using a Plane-Wave Basis set. *Phys. Rev. B* **1996**, *54*, 11169–11186, DOI: [10.1103/physrevb.54.11169](https://doi.org/10.1103/physrevb.54.11169).
- 46 Kresse, G.; Joubert, D. From Ultrasoft Pseudopotentials to the Projector Augmented-Wave Method. *Phys. Rev. B* **1999**, *59*, 1758–1775, DOI: [10.1103/physrevb.59.1758](https://doi.org/10.1103/physrevb.59.1758).
- 47 Perdew, J. P.; Burke, K.; Ernzerhof, M. Generalized gradient approximation made simple. *Physical review letters* **1996**, *77*, 3865, DOI: [10.1103/PhysRevLett.77.3865](https://doi.org/10.1103/PhysRevLett.77.3865).
- 48 Cohen, A. J.; Mori-Sánchez, P.; Yang, W. Fractional charge perspective on the band gap in density-functional theory. *Physical Review B* **2008**, *77*, DOI: [10.1103/physrevb.77.115123](https://doi.org/10.1103/physrevb.77.115123).
- 49 Crowley, J. M.; Tahir-Kheli, J.; Goddard, W. A. Resolution of the Band Gap Prediction Problem for Materials Design. *The Journal of Physical Chemistry Letters* **2016**, *7*, 1198–1203, DOI: [10.1021/acs.jpcllett.5b02870](https://doi.org/10.1021/acs.jpcllett.5b02870).
- 50 Heyd, J.; Scuseria, G. E. Efficient hybrid density functional calculations in solids: Assessment of the Heyd–Scuseria–Ernzerhof screened Coulomb hybrid functional. *The Journal of chemical physics* **2004**, *121*, 1187–1192, DOI: [10.1063/1.1760074](https://doi.org/10.1063/1.1760074).
- 51 Hummer, K.; Harl, J.; Kresse, G. Heyd-Scuseria-Ernzerhof hybrid functional for calculating the lattice dynamics of semiconductors. *Physical Review B* **2009**, *80*, 115205, DOI: [10.1103/physrevb.80.115205](https://doi.org/10.1103/physrevb.80.115205).
- 52 Monkhorst, H. J.; Pack, J. D. Special points for Brillouin-zone integrations. *Phys. Rev. B* **1976**, *13*, 5188–5192, DOI: [10.1103/PhysRevB.13.5188](https://doi.org/10.1103/PhysRevB.13.5188).
- 53 Martin, R. M. *Electronic structure: basic theory and practical methods*; Cambridge University Press, 2004.
- 54 Nosé, S. A unified formulation of the constant temperature molecular dynamics methods. *The Journal of chemical physics* **1984**, *81*, 511–519, DOI: <https://doi.org/10.1063/1.447334>.
- 55 Mostofi, A. A.; Yates, J. R.; Lee, Y.-S.; Souza, I.; Vanderbilt, D.; Marzari, N. wannier90: A tool for obtaining maximally-localised Wannier functions. *Comp. Phys. Commun.* **2008**, *178*, 685 – 699, DOI: <https://doi.org/10.1016/j.cpc.2007.11.016>.
- 56 Dias, A. C.; Silveira, J. F.; Qu, F. WanTiBEXOS: A Wannier based Tight Binding code for electronic band structure, excitonic and optoelectronic properties of solids. *Computer Physics Communications* **2023**, *285*, 108636, DOI: [10.1016/j.cpc.2022.108636](https://doi.org/10.1016/j.cpc.2022.108636).
- 57 Salpeter, E. E.; Bethe, H. A. A Relativistic Equation for Bound-State Problems. *Phys. Rev.* **1951**, *84*, 1232–1242, DOI: [10.1103/PhysRev.84.1232](https://doi.org/10.1103/PhysRev.84.1232).

- 58 Deslippe, J.; Samsonidze, G.; Strubbe, D. A.; Jain, M.; Cohen, M. L.; Louie, S. G. BerkeleyGW: A massively parallel computer package for the calculation of the quasiparticle and optical properties of materials and nanostructures. *Computer Physics Communications* **2012**, *183*, 1269–1289, DOI: [10.1016/j.cpc.2011.12.006](https://doi.org/10.1016/j.cpc.2011.12.006).
- 59 Sangalli, D.; Ferretti, A.; Miranda, H.; Attaccalite, C.; Marri, I.; Cannuccia, E.; Melo, P.; Marsili, M.; Paleari, F.; Marrazzo, A.; Prandini, G.; Bonfà, P.; Atambo, M. O.; Affinito, F.; Palumbo, M.; Molina-Sánchez, A.; Hogan, C.; Grüning, M.; Varsano, D.; Marini, A. Many-body perturbation theory calculations using the yambo code. *Journal of Physics: Condensed Matter* **2019**, *31*, 325902, DOI: [10.1088/1361-648x/ab15d0](https://doi.org/10.1088/1361-648x/ab15d0).
- 60 Pizzi, G.; Vitale, V.; Arita, R.; Blügel, S.; Freimuth, F.; Géranton, G.; Gibertini, M.; Gresch, D.; Johnson, C.; Koretsune, T.; others Wannier90 as a community code: new features and applications. *Journal of Physics: Condensed Matter* **2020**, *32*, 165902, DOI: [10.1088/1361-648X/ab51ff](https://doi.org/10.1088/1361-648X/ab51ff).
- 61 Mostofi, A. A.; Yates, J. R.; Pizzi, G.; Lee, Y.-S.; Souza, I.; Vanderbilt, D.; Marzari, N. An updated version of wannier90: A tool for obtaining maximally-localised Wannier functions. *Computer Physics Communications* **2014**, *185*, 2309–2310, DOI: [10.1016/j.cpc.2014.05.003](https://doi.org/10.1016/j.cpc.2014.05.003).
- 62 Rozzi, C. A.; Varsano, D.; Marini, A.; Gross, E. K. U.; Rubio, A. Exact Coulomb cutoff technique for supercell calculations. *Physical Review B* **2006**, *73*, DOI: [10.1103/physrevb.73.205119](https://doi.org/10.1103/physrevb.73.205119).
- 63 Pizzi, G.; Volja, D.; Kozinsky, B.; Fornari, M.; Marzari, N. BoltzWann: A code for the evaluation of thermoelectric and electronic transport properties with a maximally-localized Wannier functions basis. *Computer Physics Communications* **2014**, *185*, 422–429, DOI: [10.1016/j.cpc.2013.09.015](https://doi.org/10.1016/j.cpc.2013.09.015).
- 64 Kohn, W.; Onffroy, J. R. Wannier functions in a simple nonperiodic system. *Physical Review B* **1973**, *8*, 2485, DOI: [10.1103/PhysRevB.8.2485](https://doi.org/10.1103/PhysRevB.8.2485).
- 65 Kohn, W. Analytic properties of Bloch waves and Wannier functions. *Physical review* **1959**, *115*, 809, DOI: [10.1103/PhysRev.115.809](https://doi.org/10.1103/PhysRev.115.809).
- 66 Novikov, I. S.; Gubaev, K.; Podryabinkin, E. V.; Shapeev, A. V. The MLIP package: moment tensor potentials with MPI and active learning. *Machine Learning: Science and Technology* **2020**, *2*, 025002, DOI: [10.1088/2632-2153/abc9fe](https://doi.org/10.1088/2632-2153/abc9fe).
- 67 Mortazavi, B.; Novikov, I. S.; Podryabinkin, E. V.; Roche, S.; Rabczuk, T.; Shapeev, A. V.; Zhuang, X. Exploring phononic properties of two-dimensional materials using machine learning interatomic potentials. *Applied Materials Today* **2020**, *20*, 100685, DOI: [10.1016/j.apmt.2020.100685](https://doi.org/10.1016/j.apmt.2020.100685).
- 68 Shapeev, A. V. Moment tensor potentials: A class of systematically improvable interatomic potentials. *Multiscale Modeling & Simulation* **2016**, *14*, 1153–1173, DOI: [10.1137/15M1054183](https://doi.org/10.1137/15M1054183).
- 69 Mortazavi, B.; Silani, M.; Podryabinkin, E. V.; Rabczuk, T.; Zhuang, X.; Shapeev, A. V. First-principles multiscale modeling of mechanical properties in graphene/borophene heterostructures empowered by machine-learning interatomic potentials. *Advanced Materials* **2021**, *33*, 2102807, DOI: [10.1002/adma.202102807](https://doi.org/10.1002/adma.202102807).
- 70 Mortazavi, B.; Zhuang, X.; Rabczuk, T.; Shapeev, A. V. Atomistic modeling of the mechanical properties: the rise of machine learning interatomic potentials. *Materials Horizons* **2023**, *10*, 1956–1968, DOI: [10.1039/D3MH00125C](https://doi.org/10.1039/D3MH00125C).
- 71 Plimpton, S. Fast parallel algorithms for short-range molecular dynamics. *Journal of computational physics* **1995**, *117*, 1–19, DOI: [10.1006/jcph.1995.1039](https://doi.org/10.1006/jcph.1995.1039).

- 72 Verlet, L. Computer" experiments" on classical fluids. I. Thermodynamical properties of Lennard-Jones molecules. *Physical review* **1967**, *159*, 98, DOI: [10.1103/PhysRev.159.98](https://doi.org/10.1103/PhysRev.159.98).
- 73 Hoover, W. G. Canonical dynamics: Equilibrium phase-space distributions. *Physical review A* **1985**, *31*, 1695, DOI: [10.1103/PhysRevA.31.1695](https://doi.org/10.1103/PhysRevA.31.1695).
- 74 Nair, R. R.; Blake, P.; Grigorenko, A. N.; Novoselov, K. S.; Booth, T. J.; Stauber, T.; Peres, N. M. R.; Geim, A. K. Fine Structure Constant Defines Visual Transparency of Graphene. *Science* **2008**, *320*, 1308–1308, DOI: [10.1126/science.1156965](https://doi.org/10.1126/science.1156965).
- 75 Shockley, W.; Queisser, H. J. Detailed Balance Limit of Efficiency of p-n Junction Solar Cells. *J. Appl. Phys.* **1961**, *32*, 510–519, DOI: [10.1063/1.1736034](https://doi.org/10.1063/1.1736034).
- 76 Yu, L.; Zunger, A. Identification of Potential Photovoltaic Absorbers Based on First-Principles Spectroscopic Screening of Materials. *Phys. Rev. Lett.* **2012**, *108*, 068701, DOI: [10.1103/PhysRevLett.108.068701](https://doi.org/10.1103/PhysRevLett.108.068701).
- 77 Bernardi, M.; Palummo, M.; Grossman, J. C. Extraordinary Sunlight Absorption and One Nanometer Thick Photovoltaics Using Two-Dimensional Monolayer Materials. *Nano Letters* **2013**, *13*, 3664, DOI: [10.1021/nl401544y](https://doi.org/10.1021/nl401544y).
- 78 Standard, A. G173-03-standard tables for reference solar spectral irradiances: Direct normal and hemispherical on 37 tilted surface. *Ann. Book of ASTM Standards 2003* **2012**, *14*, 1–20, DOI: [10.1520/g0173-03r20](https://doi.org/10.1520/g0173-03r20).
- 79 Moujaes, E. A.; Dias, A. C. On the excitonic effects of the 1T and 1OT phases of PdS<sub>2</sub>, PdSe<sub>2</sub>, and PdSSe monolayers. *Journal of Physics and Chemistry of Solids* **2023**, *182*, 111573, DOI: [10.1016/j.jpcs.2023.111573](https://doi.org/10.1016/j.jpcs.2023.111573).
- 80 Jariwala, D.; Davoyan, A. R.; Wong, J.; Atwater, H. A. Van der Waals Materials for Atomically-Thin Photovoltaics: Promise and Outlook. *ACS Photonics* **2017**, *4*, 2962–2970, DOI: [10.1021/acsp Photonics.7b01103](https://doi.org/10.1021/acsp Photonics.7b01103).
- 81 Goldsmid, H. J.; others *Introduction to thermoelectricity*; Springer, 2010; Vol. 121.
- 82 Snyder, G. J.; Toberer, E. S. Complex thermoelectric materials. *Nature materials* **2008**, *7*, 105–114, DOI: [10.1038/nmat2090](https://doi.org/10.1038/nmat2090).
- 83 Harris, S. *An introduction to the theory of the Boltzmann equation*; Courier Corporation, 2004.
- 84 Jones, W.; March, N. H. *Theoretical solid state physics*; Courier Corporation, 1985; Vol. 35.
- 85 Togo, A.; Chaput, L.; Tanaka, I. Distributions of phonon lifetimes in Brillouin zones. *Physical review B* **2015**, *91*, 094306, DOI: [10.1103/PhysRevB.91.094306](https://doi.org/10.1103/PhysRevB.91.094306).
- 86 Togo, A.; Chaput, L.; Tadano, T.; Tanaka, I. Implementation strategies in phonopy and phono3py. *Journal of Physics: Condensed Matter* **2023**, *35*, 353001, DOI: [10.1088/1361-648X/acd831](https://doi.org/10.1088/1361-648X/acd831).
- 87 Morelli, D. T.; Slack, G. A. High lattice thermal conductivity solids. In *High thermal conductivity materials*; Springer, 2006; pp 37–68.
- 88 Slack, G. A. Thermal conductivity of elements with complex lattices: B, P, S. *Physical Review* **1965**, *139*, A507, DOI: [10.1103/PhysRev.139.A507](https://doi.org/10.1103/PhysRev.139.A507).
- 89 Slack, G. A. Nonmetallic crystals with high thermal conductivity. *Journal of Physics and Chemistry of Solids* **1973**, *34*, 321–335, DOI: [https://doi.org/10.1016/0022-3697\(73\)90092-9](https://doi.org/10.1016/0022-3697(73)90092-9).
- 90 Raval, D.; Moujaes, E. A.; Gupta, S. K.; Gajjar, P. Novel Penta-GeC<sub>5</sub> Nanosheet as Potential candidate for Efficient Thermoelectric Application: A DFT approach. *Journal of Physics and Chemistry of Solids* **2024**, 112157, DOI: [10.1016/j.jpcs.2024.112157](https://doi.org/10.1016/j.jpcs.2024.112157).

- 91 Sanditov, D.; Mantatov, V.; Darmaev, M.; Sanditov, B. On the Grüneisen parameter for crystals and glasses. *Technical Physics* **2009**, *54*, 385–388, DOI: [10.1134/S1063784209030098](https://doi.org/10.1134/S1063784209030098).
- 92 Peng, B.; Zhang, H.; Shao, H.; Xu, Y.; Zhang, X.; Zhu, H. Thermal conductivity of monolayer MoS<sub>2</sub>, MoSe<sub>2</sub>, and WS<sub>2</sub>: interplay of mass effect, interatomic bonding and anharmonicity. *RSC advances* **2016**, *6*, 5767–5773, DOI: [10.1039/C5RA19747C](https://doi.org/10.1039/C5RA19747C).
- 93 Julian, C. L. Theory of heat conduction in rare-gas crystals. *Physical Review* **1965**, *137*, A128, DOI: [10.1103/PhysRev.137.A128](https://doi.org/10.1103/PhysRev.137.A128).
- 94 Qin, G.; Huang, A.; Liu, Y.; Wang, H.; Qin, Z.; Jiang, X.; Zhao, J.; Hu, J.; Hu, M. High-throughput computational evaluation of lattice thermal conductivity using an optimized Slack model. *Materials Advances* **2022**, *3*, 6826–6830, DOI: [10.1039/D2MA00694D](https://doi.org/10.1039/D2MA00694D).
- 95 Mises, R. v. Mechanik der festen Körper in plastisch-deformablen Zustand. *Math.-phys. Klasse* **1913**, *4*, 582–592.
- 96 Pereira Junior, M. L.; Ribeiro Junior, L. A.; Brandão, W. H.; Aguiar, A. L.; Galvão, D. S.; De Sousa, J. M. Temperature effects on the fracture dynamics and elastic properties of popgraphene membranes. *ChemPhysChem* **2020**, *21*, 1918–1924, DOI: [10.1002/cphc.202000403](https://doi.org/10.1002/cphc.202000403).
- 97 Júnior, M. L. P.; Júnior, L. A. R. Thermomechanical insight into the stability of nanoporous graphene membranes. *FlatChem* **2020**, *24*, 100196, DOI: [10.1016/j.flatc.2020.100196](https://doi.org/10.1016/j.flatc.2020.100196).
- 98 Pereira, M.; Da Cunha, W.; De Sousa, R.; Nze, G. A.; Galvão, D.; Ribeiro, L. On the mechanical properties and fracture patterns of the nonbenzenoid carbon allotrope (biphenylene network): a reactive molecular dynamics study. *Nanoscale* **2022**, *14*, 3200–3211, DOI: [10.1039/D1NR07959J](https://doi.org/10.1039/D1NR07959J).